

<https://doi.org/10.1038/s43247-024-01380-0>

# High-frequency climate forcing causes prolonged cold periods in the Holocene

Check for updates

Evelien J. C. van Dijk<sup>1,2</sup> , Johann Jungclaus<sup>3</sup>, Michael Sigl<sup>2</sup>, Claudia Timmreck<sup>3</sup> & Kirstin Krüger<sup>1</sup>

Understanding climate variability across interannual to centennial timescales is critical, as it encompasses the natural range of climate fluctuations that early human agricultural societies had to adapt to. Deviations from the long-term mean climate are often associated with both societal collapse and periods of prosperity and expansion. Here, we show that contrary to what global paleoproxy reconstructions suggest, the mid to late-Holocene was not a period of climate stability. We use mid- to late-Holocene Earth System Model simulations, forced by state-of-the-art reconstructions of external climate forcing to show that eleven long-lasting cold periods occurred in the Northern Hemisphere during the past 8000 years. These periods correlate with enhanced volcanic activity, where the clustering of volcanic eruptions induced a prolonged cooling effect through gradual ocean-sea ice feedback. These findings challenge the prevailing notion of the Holocene as a period characterized by climate stability, as portrayed in multi-proxy climate reconstructions. Instead, our simulations provide an improved representation of amplitude and timing of temperature variations on sub-centennial timescales.

For the last 800 years, large-scale climate variability has been fairly well understood with good agreement between proxy-based climate reconstructions and climate model simulations<sup>1–4</sup>. The climate during this period is highly variable, and volcanic eruptions have been recognized as the main cause of this natural variability in the pre-industrial era<sup>5–7</sup>, culminating in glacier advances during the last phase of the Little Ice Age (LIA)<sup>8,9</sup>. In the first millennium of the Common Era (CE), paleoproxy records become more sparse<sup>10</sup>, introducing biases in reconstructions of global mean temperatures<sup>11,12</sup>. However, available regional proxy reconstructions show multi-decadal climate variability, consistent with transient climate model simulations for the past 2000 years<sup>13</sup>. From high-resolution proxy reconstructions, e.g., tree-ring records, as well as from climate model simulations, extremely cold years and decades have been distinguished in the Northern Hemisphere (NH) during the CE<sup>14,15</sup>. The coldest of these periods are identified during the mid-sixth century<sup>7,13,16</sup> and the LIA<sup>9</sup>, and these cold periods had severe societal impacts throughout the NH<sup>17,18</sup>. The LIA, starting in the period between the 13th and 15th centuries CE, and which ended around 1850 CE, is the best-known cold period, and became the eponym for comparable periods further back in time<sup>19,20</sup>. Climate model simulations in addition provide insight into the mechanisms behind periods of long-lasting cooling. Previous studies identified the atmosphere–

ocean–sea ice interaction to play a key role in the prolonged cooling after volcanic eruptions during the CE<sup>13,21–24</sup>.

Our knowledge of the large-scale annual to centennial climate variability farther back in time during the Holocene is even more limited. Existing multi-proxy reconstructions<sup>25,26</sup> are not able to fully resolve natural climate amplitudes on such timescales, due to the limited number of proxies, spatial, and seasonal biases, as well as low age precision or dating biases<sup>7,11,12,27–29</sup>. Previously, this has been portrayed as a general absence of global-scale warm or cold periods, such as the LIA, in global multi-proxy reconstructions<sup>27</sup>. In particular, multi-proxy reconstructions extending throughout the Holocene are characterized by low sampling resolution and limited age control in the underlying proxies<sup>25,26,30</sup>. In contrast, on regional scales there is growing evidence of long-lasting cold periods (multi-decadal to multi-centennial timescales) obtained from high-resolution records throughout the NH<sup>31–36</sup>. These long-lasting cold periods are typically attributed to changes in volcanic, solar, or meltwater forcing, or to changes in the Atlantic meridional overturning circulation<sup>20,37</sup>. In this study, LIA-like events are defined as long-lasting cold events (centennial scale).

High-frequency forcing like the quasi-random emission of sulfate aerosols from volcanic eruptions has rarely been included in Holocene climate model simulations<sup>38–40</sup> or data assimilations<sup>41,42</sup>. The few studies

<sup>1</sup>Department of Geosciences, University of Oslo, Oslo, Norway. <sup>2</sup>Physics Institute and Oeschger Center for Climate Change Research, University of Bern, Bern, Switzerland. <sup>3</sup>Max Planck Institute for Meteorology, Hamburg, Germany. e-mail: [e.van.dijk@geo.uio.no](mailto:e.van.dijk@geo.uio.no); [kirstin.kruger@geo.uio.no](mailto:kirstin.kruger@geo.uio.no)

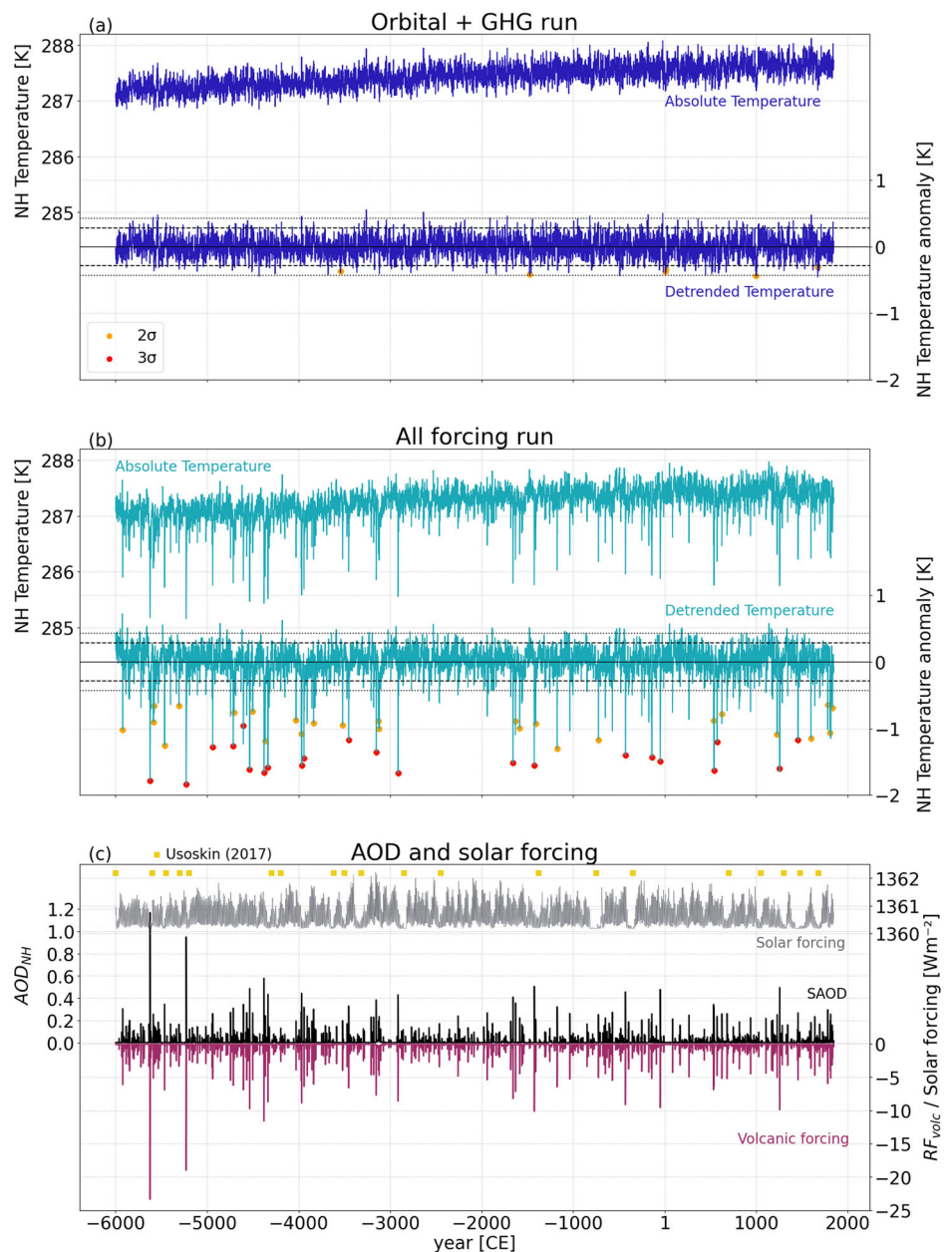
that included volcanic forcing employed simplified estimates based on only one or two ice cores, with imprecise dating, synchronization, and spatial representation<sup>43–45</sup>. Here, with a comprehensive Holocene climate model study using the Max Planck Institute Earth System Model (MPI-ESM)<sup>43,46</sup>, including a new solar irradiance record<sup>43</sup> and new reconstructions of volcanic forcing<sup>47,48</sup>, we can now study the impact of high-frequency climate forcing on the annual to centennial-scale climate variability over the past 8000 years. Over the length of this period, volcanic forcing has three main characteristics. Firstly, there is a slight but significant linear decrease of stratospheric aerosol optical depth (AOD,  $p < 0.05$ ). Secondly, strong variations between periods of relatively high eruption activity and periods of relative quiescence (similar to previously described periods such as the Medieval<sup>49</sup> or Roman<sup>50</sup> warm periods) are present. Finally, this mid to late-Holocene period is punctuated by some extreme events with magnitudes up to three times larger than the largest eruptions during the CE<sup>48</sup>. In this study, we focus on the NH, due to the limited abundance of proxies for the Southern Hemisphere for cross-comparison.

## Results and discussion

### High-frequency climate forcing and cold periods

To understand how forcing agents influence the high-frequency climate variability, we analyze the MPI-ESM Holocene runs (6000 BCE to 1850 CE)<sup>47</sup>. One run (orbital + GHG) is forced with orbital fluctuations and greenhouse gas (GHG) concentrations only, and one (all forcing) includes in addition land use, stratospheric ozone, solar irradiance, and volcanic forcing<sup>48</sup> (Methods). High-frequency climate forcing, and especially volcanic forcing, has a large impact on the 2 m air temperature (from here on temperature). This becomes evident from the differences between the Holocene orbital + GHG and the all forcing runs, in comparison with the NH aerosol optical depth (AOD<sub>NH</sub>) (Fig. 1). In contrast to the orbital + GHG run, the all forcing run produces frequent cold anomalies lasting between one and eight years. Multiyear cold periods are defined as periods with more than two consecutive years exceeding the  $2\sigma$  or  $3\sigma$  levels of the Holocene orbital + GHG, which is used here as a control experiment. The first year of each such period is highlighted in Fig. 1a, c ( $2\sigma$ , orange dots or  $3\sigma$ , red dots, Section 3). For the all forcing run, 48

**Fig. 1 | Holocene NH 2 m air temperature and high-frequency forcing.** Absolute and anomaly (detrended) for the (a) orbital + GHG run and the (b) all forcing run. The orange dots represent the starting year of a multiyear cooling outside the  $2\sigma$  range (gray dashed lines), and the red dots represent the starting year of a multiyear cooling outside the  $3\sigma$  range (gray dotted lines). c shows the NH volcanic (AOD, black), net radiative volcanic forcing (purple), total solar irradiance (gray), and the grand solar minima<sup>61</sup> (yellow squares).



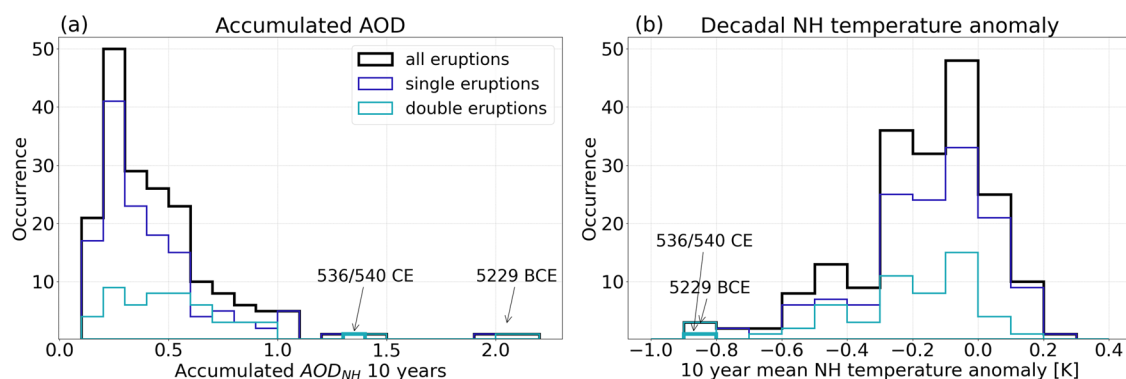
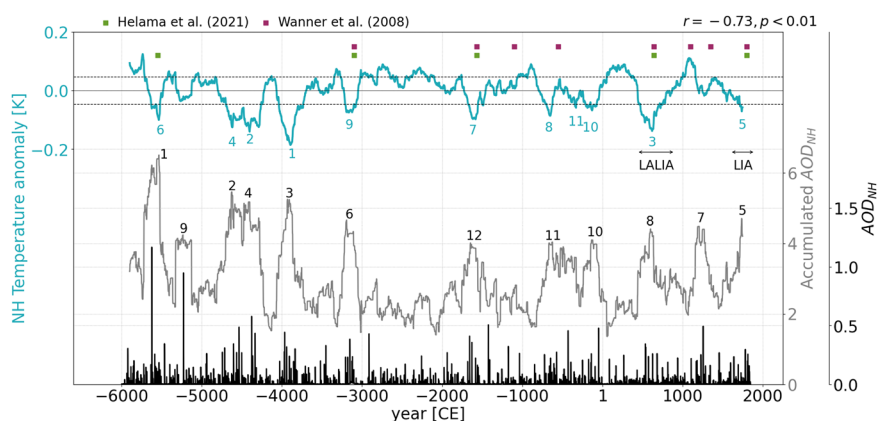


**Fig. 2 | Distribution of occurrence of 10-year mean AOD and temperature anomalies.** a Decadal AOD<sub>NH</sub> and (b) 10-year mean 2 m air temperature anomalies after eruptions with AOD<sub>NH</sub> > 0.08. The eruptions are categorized by all eruptions

(black), single eruptions (blue), and double eruptions (occurring within 10 years, teal). The 536/540 CE double-eruption event is indicated with an arrow and a thicker line.

**Fig. 3 | 200-year running mean 2 m air temperature anomaly and AOD.** Temperature anomaly (teal), accumulated AOD<sub>NH</sub> (gray), and annual mean AOD<sub>NH</sub> (black) for the Holocene run. The horizontal dashed lines represent the 2σ for the 200-year filtered orbital + GHG run. The periods with the highest accumulated 2 m air temperature and AOD<sub>NH</sub> are numbered. The green squares next to the coldest periods indicate periods found in tree-ring records from northern Finland<sup>10</sup>, and the purple squares indicate NH glacier advances as reported by ref. 58. The LALIA and the LIA are marked with an arrow.



multiyear cold periods were identified, all related to large volcanic eruptions (Fig. S1), compared to only six in the orbital + GHG run at the 2σ levels.

The duration of the surface cooling and the strength of the volcanic eruption (here in terms of its AOD value) are positively correlated. To account for multiple eruptions occurring within one cold period, the 10-year accumulated AOD<sub>NH</sub> is compared against the length of the surface cooling. The duration of the cooling is proportional to the accumulated AOD. The stronger the decadal AOD<sub>NH</sub> is, the longer the cooling lasts, especially for 3σ cooling events (Fig. S2). The volcanic forcing in the all forcing run has a greater magnitude in terms of radiative forcing than solar forcing (Fig. 1). Indeed, no significant correlation between the temperature and the solar irradiance was found (r of 0.06, compared to r of -0.6 for temperature and volcanic forcing). The exception to this is for the largest grand solar minima, like the Spörer and Maunder minima (1390–1560 and 1620–1720 CE, respectively<sup>51</sup>). During these periods the mean volcanic and solar forcing are on the same order of magnitude (-0.32 and -0.23 Wm<sup>-2</sup>, respectively for the Maunder minimum). In our simulation, land use change<sup>52</sup> starts from 850 CE, and has therefore only an influence on the last 1000 years of the all forcing run. Volcanic forcing is thus imperative to explain cold extremes in the climate of the Holocene.

### Volcanic double events

Double eruptions or cluster eruptions, such as in the 13th, mid-15th, and early 18th centuries, are thought to have a more profound and longer-lasting impact on the surface climate than single eruptions<sup>9,13,16,22,23,53–56</sup>. In particular, the 536 CE and 540 CE double-eruption events produced the largest decadal NH forcing of the last 2000 years<sup>7,13,16,57</sup>. In this study, we define volcanic double events as large volcanic eruptions (annual mean of AOD<sub>NH</sub> > 0.08) occurring within 10 years of each other. For comparison,

the double event of the 1809 (Unidentified Event) and the 1815 Tambora eruptions have an AOD<sub>NH</sub> of 0.20 and 0.26, respectively. Comparing large double events to large single eruptions (cumulative decadal AOD<sub>NH</sub> > 0.6) reveals that the double-eruption events produce up to 10 years of significant cooling on the NH, compared to five years for single eruptions (Fig. S3). The all forcing Holocene simulation shows the strongest NH decadal cooling of the last 8000 years around 5230 BCE (Fig. 2). This corresponds to the second largest NH decadal forcing, following the largest eruption of the Holocene in 5229 BCE (Unknown Event). Although it is not associated with the strongest annual forcing, the 536/540 CE double-eruption event still stands out as one of the largest decadal-scale temperature perturbations for the Holocene (Fig. 2). In addition, the cooling is the third strongest during the mid-to late-Holocene. This double-eruption event in the mid-sixth century is therefore not only in the CE, but also in the context of the Holocene an exceptional event.

### Multi-centennial cold periods in the Holocene

Two long-lasting cold periods occurred during the CE. The cold period following the 536/540 CE double-eruption event has been called the Late Antiquity Little Ice Age (LALIA)<sup>19</sup> and has been compared to the LIA in the 14th–19th centuries<sup>18</sup>. However, major differences exist between these periods regarding duration, strength, and seasonality of the cooling, and the abruptness of their onset and termination, respectively. To increase our understanding of such periods during the Holocene, we analyze the 200-year running mean temperature anomalies and compare them to the 200-year accumulated AOD<sub>NH</sub>.

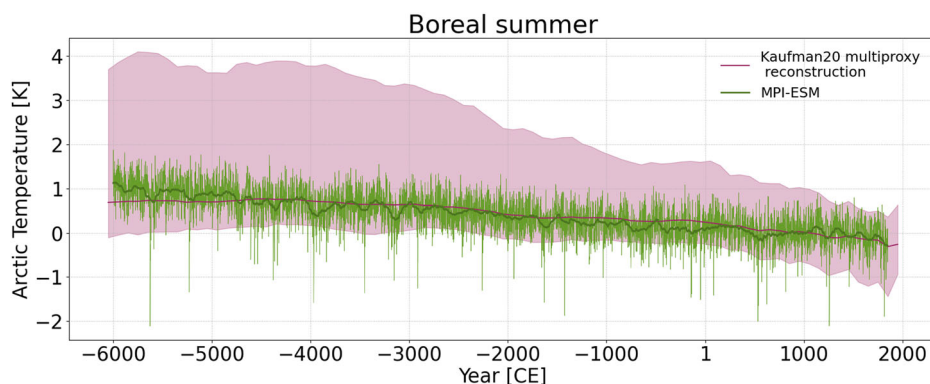
Eleven multi-centennial cold periods are identified in the temperature anomaly (detrended temperature) for the all forcing run (Fig. 3; Table 1). Of those 11 cold periods, 10 correspond to periods with the highest

**Table 1 | Information for the long-lasting cold periods**

Temperature ranking	Name cold period	Period	Nr. eruptions > Pinatubo	Most prominent eruptions Tropical/NH Extratropical/Largest
6	7.6 ka event	5637–5437 BCE	20	5635, <u>5624</u> (Mt. Mazama), 5534, 5465 BCE
4	6.6 ka event	4718–4518 BCE	19	4715, 4604, <u>4565</u> , <u>4535</u> BCE
2	6.4 ka event	4503–4303 BCE	26	4502, <u>4378</u> , 4364, 4335 BCE
1	5.9 ka event	3995–3795 BCE	23	3971, 3965, <u>3941</u> , 3836 BCE
9	5.1 ka event	3270–3070 BCE	20	3206, 3178, <u>3152</u> , 3120 BCE
7	3.6 ka event	1683–1483 BCE	22	1681, 1654, <u>1628</u> (Aniachak II), 1562 BCE
8	2.6 ka event	754–554 BCE	15	723, 648, 605, 582, <u>571</u> BCE
11	2.4 ka event	429–229 BCE	17	<u>426</u> , 393, 249 BCE
10	2.1 ka event	228–28 BCE	22	172, 144, 139, <u>43</u> (Okmok) BCE
3	LALIA	520–720 CE	23	536, <u>540</u> , 573, 626, 681 CE
5	LIA	1640–1840 CE	21	<u>1783</u> (Laki), 1809, <u>1815</u> (Tambora), 1831/35 (Cosiguina) CE

Ranking of the 200-year running mean cold periods (significant on a  $2\sigma$  level), the timing of the long-lasting cold periods, the number of eruptions larger than Pinatubo that occurred during these periods, and the most prominent volcanic eruptions that occurred during the respective cold period. The largest eruption for each cold period is underlined, and NH extratropical eruptions are given in italic. Alternative names for cold periods at or around the timing of the cold periods in our simulations can be found in Table S1.

**Fig. 4 | Model—proxy comparison for the Arctic (60°–90°N).** Temperature anomaly (wrt 1–1850 CE) for the Temperature12k reconstruction<sup>26,84</sup> mean (purple) and 5–95th percentile (shading), and the model simulated annual summer mean (green thin line) as well as the 100-year summer mean (darker green line).



accumulated  $AOD_{NH}$  in the mid to late-Holocene. The 200-year mean temperature anomaly and  $AOD_{NH}$  have a strong negative correlation ( $r = -0.73$ ,  $p < 0.01$ ), which underlines the importance of volcanic eruptions for past temperature variability. The three strongest relative multi-centennial cold periods (i.e., after detrending) occur at the beginning of the mid-Holocene, starting from 6000 BCE. Large single eruptions early in the simulated period still influence the 200-year accumulated  $AOD_{NH}$  as we have seen for the 5229 BCE eruption, but the clustering of volcanic events becomes more important for the multi-centennial climate response. The LALIA corresponds to the 3th largest 200-year cooling anomaly, and the LIA corresponds to the 5th strongest cooling anomaly.

The multi-centennial cooling events corresponding to the highest accumulated  $AOD_{NH}$  events do not necessarily rank the same. The strongest multi-centennial cooling corresponds for example to the third-largest accumulated  $AOD_{NH}$  peak (Fig. 4; Table 1). The ninth-largest accumulated  $AOD_{NH}$  peak does not correspond to a multi-centennial cooling but can be explained by a single, exceptionally large volcanic eruption occurring in 5229 BCE. The 11th coldest multi-centennial cooling anomaly appears at the end of a multi-decadal period with highly elevated aerosol loading.

We project some of the coldest LIA-like periods of the Northern Hemisphere centered around 4403 and 3895 BCE, a period currently portrayed by proxy compilations as the warmest period within the Holocene. The strongest multi-centennial cold anomaly in our model simulation occurs around 3895 BCE (5.9 ka), with a 200-year mean NH cooling of up to  $-0.18$  K (Fig. 3). Six of the simulated multi-centennial cold periods correspond to known NH glacier advancements<sup>58</sup>, see Fig. 3. However, many of these glacier advancement periods had yet to be attributed to a forcing mechanism. Five LIA-like events, defined as multi-centennial cold and

clear-sky periods, are found during the mid to late-Holocene in tree-ring records from Northern Finland<sup>20</sup>. They correspond to the cold periods occurring around 620 CE, 1583 BCE, 3170 BCE, and 5537 BCE, in addition to the LIA itself (1792 CE) in our model simulation (Fig. 3, green squares). In our simulation, we find additional NH multi-centennial cold periods centered at 4618 BCE, 4403 BCE, 3895 BCE, 654 BCE, 329 BCE, and  $-128$  BCE. Most available proxy records that cover the Holocene are from specific regions, e.g., tree-ring reconstructions from Northern Finland<sup>20</sup>, and are therefore not representative of the entire NH. This could explain why the climate model uncovers several additional NH multi-centennial cold periods.

### Cooling mechanism

Previous studies that identified long-lasting cold periods all used paleoproxy reconstructions on the centennial to millennial scale<sup>20,33,58</sup>. Some of these periods have been attributed to low solar forcing, but for others, no clear explanation has been provided so far. Both volcanic forcing and solar forcing are high-frequency climate-forcing agents, and disentangling their individual impacts on the climate is challenging. However, previous studies found that the solar forcing alone is too weak to initiate such long-lasting cold periods<sup>59,60</sup>. Comparing the model simulated long-lasting cold periods to grand solar minima periods<sup>61</sup> (Figs. 1 and 3), reveals that solar minima coincide with some of the cooling events and could have contributed, but this is not the case for all long-lasting cold periods. Solar minima also occur during periods without long-lasting cooling. A more recent study investigated the role of solar forcing and volcanic forcing in climate model simulations and concluded that the impact of solar forcing is additive to the impact of volcanic forcing, but that the solar forcing is relatively small

compared to the volcanic forcing<sup>62</sup>. Volcanism in combination with positive climate feedback (like the ocean–sea ice feedback), as proposed for the CE, has also been discussed as a possible explanation for the Holocene<sup>63</sup>. However, thus far the volcanic record for the Holocene was not extensive enough to investigate this in more detail. Now, with the MPI-ESM Holocene simulation including the new volcanic forcing<sup>48</sup> we are able to identify 11 cold periods, where the integrated effect of the volcanic forcing is the main driver of these long-lasting cold periods.

LIA-like events are not only characterized by decreased NH air temperature, but also by lower global upper ocean heat content, increased Arctic sea ice extent, and reduced ocean heat transport at 60°N (Fig. S4). Sea ice variations and heat transport into the Nordic Seas are an expression of the ocean–sea ice feedback mechanism as proposed for the CE<sup>13,21–23</sup>. Moreover, cold events coincide with a weakened sub-polar gyre in the North Atlantic. A weaker than normal sub-polar gyre circulation is associated not only with reduced meridional heat transport but also with atmospheric circulation changes leading to increased blocking frequency over northern Europe<sup>64</sup>.

Having long climate simulations including all forcing also gives us the opportunity to study in more detail the dynamics of the response to high-frequency forcing change due to the background climate. However, for this, more than one simulation is needed, so this is for future studies.

### Comparison with proxy reconstructions

High-resolution, well-dated proxy reconstructions for the CE, such as tree-ring records, agree very well with the model simulated temperatures (Fig. S5). Especially on the annual to decadal scale, the modeled land-only NH boreal summer temperatures have a similar range of variability as the tree-ring reconstructed temperatures<sup>65</sup>, with synchronous cold extremes occurring in both time series, suggesting that the model represents climate variability on these timescales well. However, these reconstructions are only available for NH summer over land between 40°N–70°N and they are generally scarce before the CE.

The majority of terrestrial proxies (e.g., pollen, chironomids) used in the multi-proxy temperature reconstructions for the Holocene, such as the temperature-12k<sup>26</sup>, are sensitive to high-latitude boreal summer temperatures. In addition, the coarse temporal resolution and low dating precision of most proxies result in a lack of high-frequency temperature variability that the climate models can resolve throughout the Holocene, and well-dated proxy reconstructions can resolve for the past 800 years<sup>4</sup>. Previous work has focused on resolving a mismatch in the long-term trends of simulated and reconstructed temperature evolution over the Holocene, which has been described as 'the Holocene conundrum'<sup>45</sup>. A number of explanations have been suggested to explain and resolve the disagreement, including spatial and seasonal biases in proxy reconstructions, or imperfect representations of forcings and feedbacks in climate models<sup>30,41,43,66–69</sup>. Since our MPI simulations only start in the mid-Holocene and lack any ice-sheet and freshwater forcing, they can only provide limited insights into the Holocene temperature conundrum. Similar to other models, MPI-ESM simulates a long-term increase of annual mean temperatures, with no evidence of a global thermal maximum during the mid-Holocene, as is suggested by proxy records to have occurred around 4500 BCE. With highly increased volcanic activity during a mid-Holocene active period<sup>48</sup>, the 4700–4300 BCE period is represented by the MPI simulation as one of the coldest periods in the last 8000 years. However, when using the simulated high-latitude (60°–90°N) summer temperatures and comparing them to the 60°–90°N averaged temperature-12k reconstruction, model and proxy reconstructions agree on an overall decreasing trend. The 200-year mean modeled temperatures still remain on the lower bound of the uncertainty range for the reconstructed temperatures (Fig. 4 and S6). This lends support to previous suggestions of a warm bias in Holocene temperature reconstructions based on a spatial and seasonal sampling bias<sup>30,43</sup>.

The Holocene climate is widely described to have had relatively small magnitudes of climate change<sup>68</sup>, a notion that is based on available multi-proxy compilations of comparable coarse resolution<sup>25,26</sup> and transient model simulations lacking high-resolution volcanic forcing<sup>45</sup>. In contrast, our MPI-

ESM simulations show large climate variations on seasonal to multi-centennial timescales throughout the past 8000 years, with amplitudes on par or exceeding those in the pre-industrial CE. These larger amplitudes are expected, as both the volcanic eruption frequency and the strength of individual eruptions over the past 8000 years often exceed that of volcanic eruptions of the CE.

### Impact on society

The recurrence time of long-lasting cold periods in our climate model simulation is 700 years on average, with the exception of the 'Holocene Quiet Period' (3000 BCE to 2000 BCE)<sup>48</sup>, due to the absence of periods with increased volcanic activity (Fig. 3). Long-lasting cold periods during the mid to late-Holocene may be a contributing factor in societal change, as is proposed for the LALIA and the LIA<sup>13,16–18,28</sup>, or for the termination of the Gressbakken culture in Arctic Scandinavia during the 3.6 ka event<sup>70</sup>. For example, the cooling after the 536/540 CE double-eruption event impacted agriculture in Scandinavia, which led to the abandonment of farm sites in areas where they were vulnerable to crop failure<sup>71</sup>. In addition to long-lasting cold periods themselves having an impact on society, the rate of climate change is also an important factor<sup>33,72</sup>, as rapid climate change (RCC) gives little time for adaptation. RCC periods are defined as rapid changes in climate in the time span of a few hundred years. One example of an RCC is the change from the Medieval Warm Period, the warm period occurring around 950–1100 CE, to the LIA<sup>33</sup>. Unique with our model simulations is, that we can study the spatial pattern of the RCCs and increase our understanding of which areas could have been more impacted. In Fig. 5, the transitions, or RCC, for three periods are given. The RCC was calculated by subtracting the coldest 200-year mean period (Fig. 5b, e, h) from the warmest 200-year mean period (Fig. 5a, d, g), which resulted in the RCC rate for each transition (Fig. 5c, f, i). For the Roman warm period (the warm period around 379 CE) to the LALIA, and the 4130 to 3900 BCE transitions, we find the largest amplitudes of RCC (up to 0.8 °C) in the Barents and Kara Sea regions, reflecting the importance of sea ice feedback mechanisms (Fig. 5f, i). Our simulation illustrates that certain RCC transition periods (occurring within 300–600 years) during the mid to late-Holocene, like the transition from the Roman warm period to the LALIA, or the 3895 BCE cold period to the 3200 BCE warm period, were even more intense (0.13 °C per century) than the Medieval warm period to LIA transition. In addition, these RCC periods were most severe partly in areas with agricultural development (Fig. 5, hatched areas).

Long-lasting cold periods and the transition to and from these periods could thus have had severe consequences for people living in the NH during those events. Indeed, several studies indicate a change in societies during cold periods throughout the Holocene, besides the LIA and LALIA. For example, the period 4500 BCE to 3000 BCE has been characterized as a tumultuous period impacting societies living in the Near East, the eastern Mediterranean, and northern Africa<sup>72</sup>. This coincides with the identified long-lasting cold periods three, five, one, and nine in our climate model simulation. In Mesopotamia, settlement expansion and contraction coincided with periods of climate change around 3800 BCE and 3200 BCE<sup>72</sup>, which coincides with our prolonged cold periods one and nine. The caldera-forming eruptions of Okmok II (43 BCE) and Aniakhak II (1628 BCE) have been linked to climate extremes and societal responses in Europe<sup>70,73</sup>, which occurred during our cold periods ten and six (LIA) respectively. However, a direct causation between climate change and societal change has thus far not been proven and needs further discussion in future studies.

By illustrating how the temporal resolution of the surface temperature as represented in proxy reconstructions affects the timing and severity of cold periods, and by identifying missing cold periods compared to reconstructions, we demonstrate the limitations of the paleoclimate proxy reconstructions. In addition, there is a need for further improvements by updating proxy records to the latest chronologies, improving the age models, and filling spatial (Southern Hemisphere) and seasonal (boreal winter) gaps. Understanding the climate of the past is important to evaluate model performance and, ultimately, increase confidence in the model's

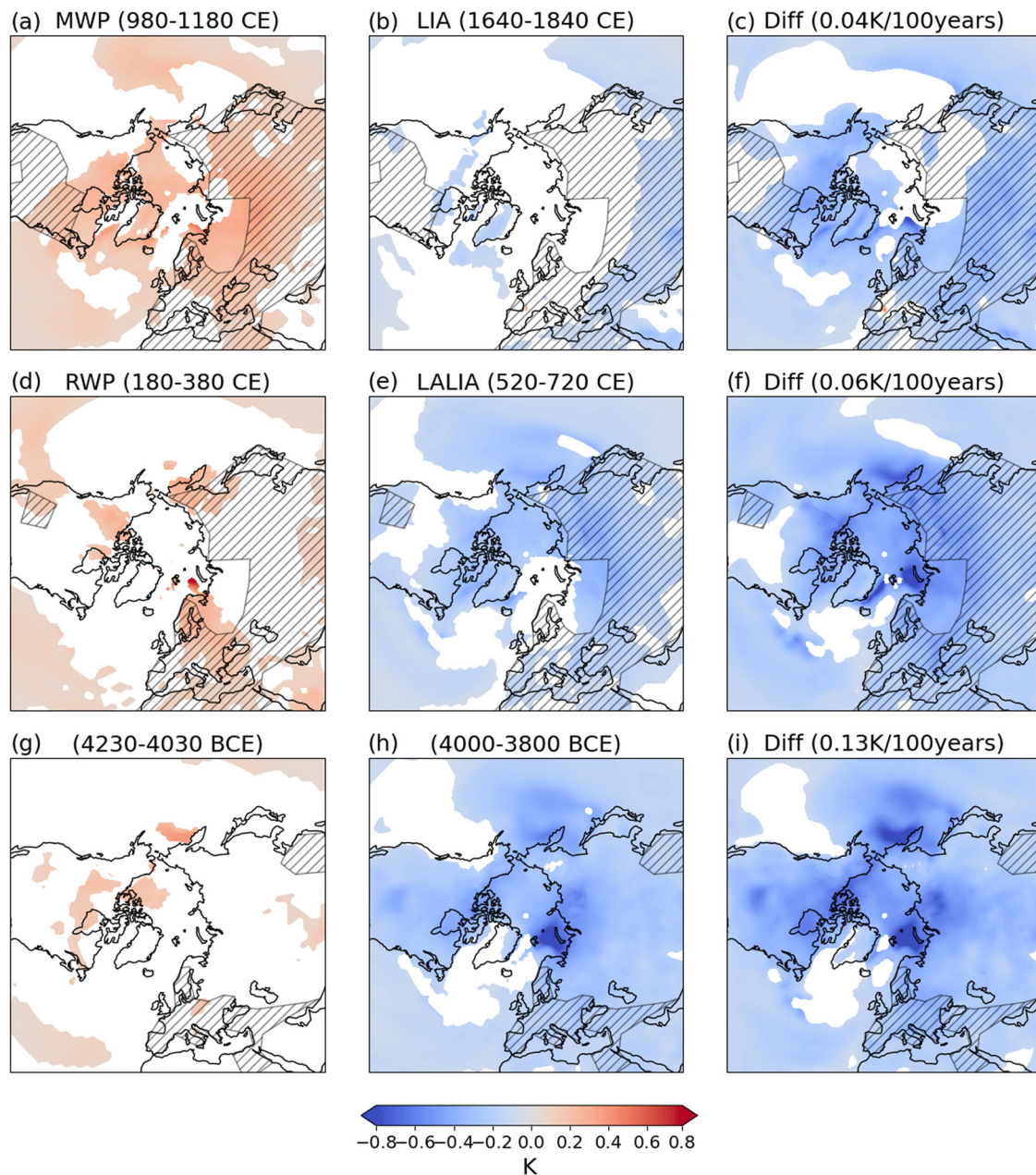


**Fig. 5 | Rapid Climate Change events during the mid to late-Holocene.** 200-year mean minimum and maximum temperature periods (based on the detrended 200-year running mean time series) for (a) the Medieval warm period (MWP) and (b) the Little Ice Age (LIA), (d) the Roman warm period (RWP) and (e) the Late Late Antiquity

Little Ice Age (LALIA), and (g) 4129 BCE warm period and (h) the 3895 BCE cold period, and their difference (c, f, and i). The gray hatching represents the areas with extensive agriculture<sup>85,86</sup>. Temperature anomalies are significant on the 2  $\sigma$  level.

future climate projections. Only a few Holocene runs with fully coupled Earth System Models and realistic volcanic forcing are available thus far<sup>47,69</sup>.

For the first time to the best of our knowledge, we employ a fully coupled earth system model simulation with new and updated volcanic forcing to study the long-lasting cold periods of the mid to late-Holocene and the possible mechanisms behind them. In the *all forcing* run, we identify 11 multi-centennial NH cold periods, similar to the LIA cold periods as identified in Northern Finland<sup>20</sup>, but here we identify six more (due to higher temporal resolution) with a recurrence time of once to twice per millennium. With climate model simulations we can in addition study the mechanism behind these cold periods. Previously, solar forcing was suggested as a possible mechanism for some of the identified cold periods from proxy data, but while grand solar minima occur during some of our long-lasting cold periods and always coincide with increased volcanic activity, this does not explain all long-lasting cold periods. The integrated effect of

volcanic forcing through the ocean–sea ice feedback does explain all identified long-lasting cold periods in the model simulation. In addition, these long-lasting cold periods might have impacted societies living at the time, especially around the Mediterranean and the Middle East.

As our results highlight, high-frequency climate forcing, and in particular volcanic forcing, is needed to resolve the full spectrum of climate variability during the Holocene, which is not present in available NH or global multi-proxy reconstructions. This is imperative for studying LIA-like events and their potential impacts on societies that existed during those times, and in the future as well.

## Methods

### Model and experiments

The MPI-ESM1.2<sup>74</sup> features a T63 horizontal resolution ( $1.9^\circ \times 1.9^\circ$ ) for the atmospheric component (ECHAM6) and a vertical resolution of 47 levels

between the surface and top of the atmosphere at 80 km (0.01 hPa)<sup>75</sup>. The ocean component (MPIOM) has a nominal horizontal resolution of 1.5° and 40 vertical levels<sup>76</sup>. Here, we use two transient simulations that span the mid to late-Holocene (6000 BCE to 1850 CE). One simulation includes prescribed variations in orbital forcing<sup>77</sup> and greenhouse gas concentrations<sup>46,78</sup> (the `orbital + GHG` run), and one simulation includes, in addition, land use changes<sup>52</sup>, stratospheric ozone (varies with solar irradiance, see<sup>43</sup>), solar irradiance<sup>79</sup> and stratospheric volcanic aerosol<sup>48</sup> (the `all forcing` run). The spin-up simulation was run with constant conditions at 6000 BCE. More information on the model setup and the Holocene run can be found in ref. 47.

The volcanic forcing used for the MPI-ESM Holocene run is the `HolVol1.0`<sup>48</sup> for the years 6000 BCE to 20 BCE, and the `eVolv2k` data set<sup>57</sup> for 20 BCE to 1850 CE. These data sets are based on the sulfur deposition from ice cores.<sup>48</sup> extended the previous volcanic records by 7000 years, creating the first monthly resolved volcanic forcing data set constrained by Greenland and Antarctic ice cores for the mid to late-Holocene, which can be used as input for climate model simulations. The easy volcanic aerosol forcing generator EVA<sup>80</sup> was applied to obtain wavelength-dependent aerosol extinction, single scattering albedo, and scattering asymmetry factor values, which were then used as input for the MPI-ESM. Here we use the stratospheric aerosol optical depth (AOD) at 550 nm as a measure for the climate impact potential of volcanic eruptions. Since there is a lack of proxy reconstructions for the Southern Hemisphere, including in the global-scale proxy records, and the main population centers are located in the NH, we focus on the climate response in the NH. Therefore, in this study we use the results for the NH mean AOD (AOD<sub>NH</sub>), which is similar to the global mean (see Fig. 9 in ref. 48).

### Classification of eruptions

Large volcanic eruptions are defined in this study as eruptions with an annual AOD<sub>NH,peak</sub> > 0.08 (Tambora has an AOD<sub>NH</sub> of 0.26). Large eruptions occurring within ten years of each other are defined as double eruptions and are removed from the list of all large eruptions, thus classifying all Holocene eruptions into single and double-eruption events.

### Statistics

For both runs, `orbital + GHG` and `all forcing`, the NH annual mean temperature is calculated. To assess the significant differences between the two runs, these temperature time series for both the `all forcing` and the `orbital + GHG` runs are detrended. The NH annual mean temperature anomalies are calculated in a similar way, by fitting a second-degree polynomial function and subtracting this from the NH annual mean. The standard deviation is calculated for the detrended `orbital + GHG` run. This standard deviation is used for the 2  $\sigma$  and 3  $\sigma$  significance levels throughout the study. To test the significance of volcanic cooling, the periods with more than 2 years exceeding 2  $\sigma$  and 3  $\sigma$  are selected and defined as multiyear cooling. A multiyear cooling with more than 2 years below 2  $\sigma$ , but not below 3  $\sigma$  is marked as a 2  $\sigma$  cooling, whereas a multiyear cooling with more than 2 years below 3  $\sigma$  is marked as a 3  $\sigma$  cooling.

The significance is calculated by applying the same filters (or running means) to the `orbital + GHG` run and deriving the standard deviation from this filtered data. To find the correlation between the temperature anomalies and the AOD<sub>NH</sub>, the Pearson Product-Moment Correlation Coefficient is defined for each filtered time series. This is a measure of the linear relationship between two random variables and is given by Equation (1):

$$\rho_{X,Y} = \frac{\sigma_{X,Y}}{\sigma_X \sigma_Y} \quad (1)$$

with  $\rho_{X,Y}$  being the covariance between X and Y, and  $\sigma_X$  and  $\sigma_Y$  being the standard deviation of X and Y, respectively. Specifically, X denotes the temperature anomalies, and Y the AOD<sub>NH</sub>. The value of  $\rho_{X,Y}$ , hereafter  $r$ , then varies between +1 and -1, with 0 indicating no correlation, +1

indicating a perfect positive correlation, and -1 indicating a perfect negative correlation.

To calculate the significance of the Pearson correlation, the  $t$ -test was carried out on the 95% confidence level.

### Data availability

The climate model output used in this study can be found on Zenodo<sup>81,82</sup> (<https://doi.org/10.5281/zenodo.10409454>). Data for the proxy reconstructions is available at the NOAA database:<sup>83</sup> <https://www.ncei.noaa.gov/access/paleo-search/study/33215> and<sup>84</sup> <https://www.ncei.noaa.gov/access/paleo-search/study/27330>. Data for the land use study can be found at Harvard Dataverse<sup>85</sup> <https://dataverse.harvard.edu/dataset.xhtml?persistentId=doi:10.7910/DVN/CQWUBI>.

### Code availability

Scripts for the calculations and post-processing of the data can be found on Zenodo (<https://doi.org/10.5281/zenodo.10692381>).

Received: 20 December 2023; Accepted: 9 April 2024;

Published online: 08 May 2024

### References

- PAGES2k. Consistent multidecadal variability in global temperature reconstructions and simulations over the Common Era. *Nat. Geosci.* **12**, 643–649 (2019).
- King, J. M. et al. A data assimilation approach to last millennium temperature field reconstruction using a limited high-sensitivity proxy network. *J. Clim.* **34**, 7091–7111 (2021).
- Smerdon, J. E., Cook, E. R. & Steiger, N. J. The historical development of large-scale paleoclimate field reconstructions over the common era. *Rev. Geophys.* **61**, e2022RG000782 (2023).
- Zhu, F., Emile-Geay, J., Hakim, G. J., King, J. & Anchukaitis, K. J. Resolving the differences in the simulated and reconstructed temperature response to volcanism. *Geophys. Res. Lett.* **47**, e2019GL086908 (2020).
- Hegerl, G. C., Crowley, T. J., Hyde, W. T. & Frame, D. J. Climate sensitivity constrained by temperature reconstructions over the past seven centuries. *Nature* **440**, 1029–1032 (2006).
- Schurer, A. P., Hegerl, G. C., Mann, M. E., Tett, S. & Phipps, S. J. Separating forced from chaotic climate variability over the past millennium. *J. Clim.* **26**, 6954–6973 (2013).
- Sigl, M. et al. Timing and climate forcing of volcanic eruptions for the past 2500 years. *Nature* **523**, 543–549 (2015).
- Solomina, O. N. et al. Glacier fluctuations during the past 2000 years. *Quat. Sci. Rev.* **149**, 61–90 (2016).
- Brönnimann, S. et al. Last phase of the Little Ice Age forced by volcanic eruptions. *Nat. Geosci.* **12**, 650–656 (2019).
- PAGES2k Consortium. A global multiproxy database for temperature reconstructions of the common era. *Sci. Data* **4**, 170088 (2017).
- Anchukaitis, K. J. & Smerdon, J. E. Progress and uncertainties in global and hemispheric temperature reconstructions of the Common Era. *Quat. Sci. Rev.* **286**, 107537 (2022).
- Büntgen, U. Scrutinizing tree-ring parameters for Holocene climate reconstructions. *Wiley Interdiscip. Rev. Clim. Chang.* **13**, e778 (2022).
- van Dijk, E., Jungclaus, J., Lorenz, S., Timmreck, C. & Krüger, K. Was there a volcanic-induced long-lasting cooling over the Northern Hemisphere in the mid-6th–7th century? *Clim. Past* **18**, 1601–1623 (2022).
- Stoffel, M. et al. Estimates of volcanic-induced cooling in the Northern Hemisphere over the past 1500 years. *Nat. Geosci.* **8**, 784–788 (2015).
- Wilson, R. et al. Last millennium northern hemisphere summer temperatures from tree rings: Part I: the long term context. *Quat. Sci. Rev.* **134**, 1–18 (2016).

16. Toohey, M., Krüger, K., Sigl, M., Stordal, F. & Svensen, H. Climatic and societal impacts of a volcanic double event at the dawn of the Middle Ages. *Clim. Chang.* **136**, 401–412 (2016).
17. Zhang, D. D., Brecke, P., Lee, H. F., He, Y.-Q. & Zhang, J. Global climate change, war, and population decline in recent human history. *Proc. Natl Acad. Sci. USA* **104**, 19214–19219 (2007).
18. Degroot, D. et al. Towards a rigorous understanding of societal responses to climate change. *Nature* **591**, 539–550 (2021).
19. Büntgen, U. et al. Cooling and societal change during the Late Antique Little Ice Age from 536 to around 660 AD. *Nat. Geosci.* **9**, 231 (2016).
20. Helama, S. et al. Recurrent transitions to Little Ice Age-like climatic regimes over the Holocene. *Clim. Dyn.* **56**, 3817–3833 (2021).
21. Zhong, Y. et al. Centennial-scale climate change from decadal-paced explosive volcanism: a coupled sea ice-ocean mechanism. *Clim. Dyn.* **37**, 2373–2387 (2011).
22. Miller, G. H. et al. Abrupt onset of the Little Ice Age triggered by volcanism and sustained by sea-ice/ocean feedbacks. *Geophys. Res. Lett.* **39** (2012).
23. Lehner, F., Born, A., Raible, C. C. & Stocker, T. F. Amplified inception of European Little Ice Age by sea ice–ocean–atmosphere feedbacks. *J. Clim.* **26**, 7586–7602 (2013).
24. Zanchettin, D. et al. Background conditions influence the decadal climate response to strong volcanic eruptions. *J. Geophys. Res. Atmos.* **118**, 4090–4106 (2013).
25. Marcott, S. A., Shakun, J. D., Clark, P. U. & Mix, A. C. A reconstruction of regional and global temperature for the past 11,300 years. *Science* **339**, 1198–1201 (2013).
26. Kaufman, D. et al. Holocene global mean surface temperature, a multi-method reconstruction approach. *Sci. Data* **7**, 1–13 (2020).
27. Neukom, R. et al. Consistent multi-decadal variability in global temperature reconstructions and simulations over the Common Era. *Nat. Geosci.* **12**, 643 (2019).
28. Büntgen, U. et al. Prominent role of volcanism in common era climate variability and human history. *Dendrochronologia* **64**, 125757 (2020).
29. Plunkett, G. et al. No evidence for tephra in Greenland from the historic eruption of Vesuvius in 79 CE: implications for geochronology and paleoclimatology. *Clim. Past* **18**, 45–65 (2022).
30. Marsicek, J., Shuman, B. N., Bartlein, P. J., Shafer, S. L. & Brewer, S. Reconciling divergent trends and millennial variations in Holocene temperatures. *Nature* **554**, 92–96 (2018).
31. Wanner, H., Solomina, O., Grosjean, M., Ritz, S. P. & Jetel, M. Structure and origin of Holocene cold events. *Quat. Sci. Rev.* **30**, 3109–3123 (2011).
32. Donges, J. F. et al. Non-linear regime shifts in Holocene Asian monsoon variability: Potential impacts on cultural change and migratory patterns. *Clim. Past* **11**, 709–741 (2015).
33. Mayewski, P. A. et al. Holocene climate variability. *Quat. Res.* **62**, 243–255 (2004).
34. Harning, D. J., Geirsdóttir, Á. & Miller, G. H. Punctuated Holocene climate of vestfirðir, iceland, linked to internal/external variables and oceanographic conditions. *Quat. Sci. Rev.* **189**, 31–42 (2018).
35. Hou, M. et al. Detection of a mid-holocene climate event at 7.2 ka bp based on an analysis of globally-distributed multi-proxy records. *Palaeogeogr. Palaeoclimatol. Palaeoecol.* **618**, 111525 (2023).
36. Lapointe, F. et al. Annually resolved Atlantic sea surface temperature variability over the past 2900 y. *Proc. Natl Acad. Sci. USA* **117**, 27171–27178 (2020).
37. Nicolussi, K. et al. A 9111 year long conifer tree-ring chronology for the European Alps: a base for environmental and climatic investigations. *Holocene* **19**, 909–920 (2009).
38. Armstrong, E., Hopcroft, P. O. & Valdes, P. J. A simulated northern hemisphere terrestrial climate dataset for the past 60,000 years. *Sci. Data* **6**, 265 (2019).
39. Braconnot, P., Zhu, D., Marti, O. & Servonnat, J. Strengths and challenges for transient mid-to late Holocene simulations with dynamical vegetation. *Clim. Past* **15**, 997–1024 (2019).
40. Wen, X., Liu, Z., Wang, S., Cheng, J. & Zhu, J. Correlation and anti-correlation of the East Asian summer and winter monsoons during the last 21,000 years. *Nat. Commun.* **7**, 11999 (2016).
41. Erb, M. P. et al. Reconstructing Holocene temperatures in time and space using paleoclimate data assimilation. *Clim. Past* **18**, 2599–2629 (2022).
42. Osman, M. B. et al. Globally resolved surface temperatures since the last glacial maximum. *Nature* **599**, 239–244 (2021).
43. Bader, J. et al. Global temperature modes shed light on the Holocene temperature conundrum. *Nat. Commun.* **11**, 1–8 (2020).
44. Kobashi, T. et al. Volcanic influence on centennial to millennial Holocene Greenland temperature change. *Sci. Rep.* **7**, 1–10 (2017).
45. Liu, Z. et al. The Holocene temperature conundrum. *Proc. Natl Acad. Sci. USA* **111**, E3501–E3505 (2014).
46. Brovkin, V. et al. What was the source of the atmospheric CO<sub>2</sub> increase during the Holocene? *Biogeosciences* **16**, 2543–2555 (2019).
47. Dallmeyer, A. et al. Holocene vegetation transitions and their climatic drivers in MPI-ESM1. 2. *Clim. Past* **17**, 2481–2513 (2021).
48. Sigl, M., Toohey, M., McConnell, J. R., Cole-Dai, J. & Severi, M. Volcanic stratospheric sulfur injections and aerosol optical depth during the Holocene (past 11 500 years) from a bipolar ice-core array. *Earth Syst. Sci. Data* **14**, 3167–3196 (2022).
49. Bradley, R. S., Wanner, H. & Diaz, H. F. The medieval quiet period. *Holocene* **26**, 990–993 (2016).
50. Manning, J. G. et al. Volcanic suppression of Nile summer flooding triggers revolt and constrains interstate conflict in ancient Egypt. *Nat. Commun.* **8**, 900 (2017).
51. Brehm, N. et al. Eleven-year solar cycles over the last millennium revealed by radiocarbon in tree rings. *Nat. Geosci.* **14**, 10–15 (2021).
52. Hurtt, G. C. et al. Harmonization of global land use change and management for the period 850–2100 (LUH2) for CMIP6. *Geosci. Model Dev.* **13**, 5425–5464 (2020).
53. Briffa, K. R., Jones, P. D., Schweingruber, F. H. & Osborn, T. J. Influence of volcanic eruptions on Northern Hemisphere summer temperature over the past 600 years. *Nature* **393**, 450–455 (1998).
54. Sigl, M. et al. A new bipolar ice core record of volcanism from WAIS divide and NEEM and implications for climate forcing of the last 2000 years. *J. Geophys. Res. Atmos.* **118**, 1151–1169 (2013).
55. Gupta, M. & Marshall, J. The climate response to multiple volcanic eruptions mediated by ocean heat uptake: damping processes and accumulation potential. *J. Clim.* **31**, 8669–8687 (2018).
56. Timmreck, C. et al. The unidentified eruption of 1809: a climatic cold case. *Clim. Past* **17**, 1455–1482 (2021).
57. Toohey, M. & Sigl, M. Volcanic stratospheric sulphur injections and aerosol optical depth from 500 BCE to 1900 CE. *Earth Syst. Sci. Data* **9**, 809–831 (2017).
58. Wanner, H. et al. Mid-to Late Holocene climate change: an overview. *Quat. Sci. Rev.* **27**, 1791–1828 (2008).
59. Gray, L. J. et al. Solar influences on climate. *Rev. Geophys.* **48** (2010).
60. Owens, M. J. et al. The Maunder minimum and the Little Ice Age: an update from recent reconstructions and climate simulations. *J. Space Weather Space Clim.* **7**, A33 (2017).
61. Usoskin, I. G. A history of solar activity over millennia. *Living Rev. Sol. Phys.* **14**, 3 (2017).
62. Fang, S.-W., Timmreck, C., Jungclaus, J., Krüger, K. & Schmidt, H. On the additivity of climate responses to the volcanic and solar forcing in the early 19th century. *Earth Syst. Dyn.* **13**, 1535–1555 (2022).
63. Solomina, O. N. et al. Holocene glacier fluctuations. *Quat. Sci. Rev.* **111**, 9–34 (2015).
64. Moreno-Chamarro, E., Zanchettin, D., Lohmann, K., Luterbacher, J. & Jungclaus, J. H. Winter amplification of the European Little Ice Age cooling by the subpolar gyre. *Sci. Rep.* **7**, 1–8 (2017).



65. Büntgen, U. et al. The influence of decision-making in tree ring-based climate reconstructions. *Nat. Commun.* **12**, 1–10 (2021).
66. Bova, S., Rosenthal, Y., Liu, Z., Godad, S. P. & Yan, M. Seasonal origin of the thermal maxima at the Holocene and the last interglacial. *Nature* **589**, 548–553 (2021).
67. Thompson, A. J., Zhu, J., Poulsen, C. J., Tierney, J. E. & Skinner, C. B. Northern hemisphere vegetation change drives a Holocene thermal maximum. *Sci. Adv.* **8**, eabj6535 (2022).
68. Kaufman, D. S. & Broadman, E. Revisiting the Holocene global temperature conundrum. *Nature* **614**, 425–435 (2023).
69. Hopcroft, P. O., Valdes, P. J., Shuman, B. N., Toohey, M. & Sigl, M. Relative importance of forcings and feedbacks in the Holocene temperature conundrum. *Quat. Sci. Rev.* **319**, 108322 (2023).
70. Jørgensen, E. K. & Riede, F. Convergent catastrophes and the termination of the Arctic Norwegian Stone Age: a multi-proxy assessment of the demographic and adaptive responses of mid-Holocene collectors to biophysical forcing. *Holocene* **29**, 1782–1800 (2019).
71. van Dijk, E. et al. Climate and societal impacts in Scandinavia following the 536 and 540 CE volcanic double event. *Clim. Past* **19**, 357–398 (2023).
72. Clarke, J. et al. Climatic changes and social transformations in the Near East and North Africa during the 'long' 4th millennium BC: a comparative study of environmental and archaeological evidence. *Quat. Sci. Rev.* **136**, 96–121 (2016).
73. McConnell, J. R. et al. Extreme climate after massive eruption of Alaska's Okmok volcano in 43 BCE and effects on the late Roman Republic and Ptolemaic Kingdom. *Proc. Natl Acad. Sci. USA* **117**, 15443–15449 (2020).
74. Mauritsen, T. et al. Developments in the MPI-M earth system model version 1.2 (MPI-ESM1.2) and its response to increasing CO<sub>2</sub>. *J. Adv. Model. Earth Syst.* **11**, 998–1038 (2019).
75. Stevens, B. et al. Atmospheric component of the MPI-M Earth system model: ECHAM6. *J. Adv. Model. Earth Syst.* **5**, 146–172 (2013).
76. Jungclaus, J. et al. Characteristics of the ocean simulations in the Max Planck Institute Ocean Model (MPIOM) the ocean component of the MPI-Earth system model. *J. Adv. Model. Earth Syst.* **5**, 422–446 (2013).
77. Berger, A. L. Long-term variations of caloric insolation resulting from the Earth's orbital elements 1. *Quat. Res.* **9**, 139–167 (1978).
78. Köhler, P. Interactive comment on "What was the source of the atmospheric CO<sub>2</sub> increase during the Holocene?" by Victor Brovkin et al. *Biogeosci. Discuss.* **16**, SC1 (2019).
79. Krivova, N., Solanki, S. & Unruh, Y. Towards a long-term record of solar total and spectral irradiance. *J. Atmos. Solar-Terrest. Phys.* **73**, 223–234 (2011).
80. Toohey, M., Stevens, B., Schmidt, H. & Timmreck, C. Easy Volcanic Aerosol (EVA v1.0): an idealized forcing generator for climate simulations. *Geosci. Model Dev.* **9**, 4049–4070 (2016).
81. van Dijk, E., Timmreck, C. & Jungclaus, J. MPI-ESM Holocene simulations dataset for 'High-frequency climate forcing causes prolonged cold periods in the Holocene'. <https://doi.org/10.5281/zenodo.10409454> (2023).
82. van Dijk, E. Scripts for 'High-frequency climate forcing causes prolonged cold periods in the Holocene'. <https://doi.org/10.5281/zenodo.10692382> (2024).
83. Buntgen, U. Northern Hemisphere 2000 year tree-ring ensemble temperature reconstructions. <https://www.ncel.noaa.gov/access/paleo-search/study/33215> (2021).
84. Kaufman, D., McKay, N. & Routson, C. Temperature 12k database. <https://www.ncel.noaa.gov/access/paleo-search/study/27330> (2020).
85. Project, A. ArchaeoGLOBE regions. <https://doi.org/10.7910/DVN/CQWUBI> (2018).
86. Stephens, L. et al. Archaeological assessment reveals Earth's early transformation through land use. *Science* **365**, 897–902 (2019).

## Acknowledgements

This study is funded by the NFR TOPPFORSK project "VIKINGS" (grant no. 275191) at the University of Oslo. Evelien Van Dijk and Michael Sigl received funding from the the NFR TOPPFORSK project "VIKINGS" (grant no. 275191) at the University of Oslo, and also from the European Research Council under the European Union's Horizon 2020 research and innovation program ("THERA", grant agreement no. 820047). Claudia Timmreck acknowledges support by the Deutsche Forschungsgemeinschaft Research Unit VollImpact (FOR2820 (grant no. 398006378)). Computations, analysis, and model data storage were mainly performed on the computer of the Deutsches Klima Rechenzentrum (DKRZ) and partly on the Sigma2 the National Infrastructure for High-Performance Computing and Data Storage in Norway. Primary scripts used in the analysis and the other supplementary information that may be useful in reproducing the author's work are archived and can be obtained by request. We would like to thank Stephan Lorenz for conducting the MPI-ESM Holocene runs, and Robert O. David, Tim Carlsen and Herman Fuglestedt for constructive discussions.

## Author contributions

E.v.D., K.K., M.S. and C.T. conceived the original idea. E.v.D. processed the data, performed the analysis, designed the figures, and wrote the paper. K.K., M.S., C.T. and J.J. contributed to the interpretation and discussion of the results and helped write the manuscript. K.K. supervised the project.

## Competing interests

The authors declare no competing interests.

## Additional information

**Supplementary information** The online version contains supplementary material available at <https://doi.org/10.1038/s43247-024-01380-0>.

**Correspondence** and requests for materials should be addressed to Evelien J. C. van Dijk or Kirstin Krüger.

**Peer review information** *Communications Earth & Environment* thanks the anonymous reviewers for their contribution to the peer review of this work. Primary handling editors: Rachael Rhodes and Aliénor Lavergne. A peer review file is available.

**Reprints and permissions information** is available at <http://www.nature.com/reprints>

**Publisher's note** Springer Nature remains neutral with regard to jurisdictional claims in published maps and institutional affiliations.

**Open Access** This article is licensed under a Creative Commons Attribution 4.0 International License, which permits use, sharing, adaptation, distribution and reproduction in any medium or format, as long as you give appropriate credit to the original author(s) and the source, provide a link to the Creative Commons licence, and indicate if changes were made. The images or other third party material in this article are included in the article's Creative Commons licence, unless indicated otherwise in a credit line to the material. If material is not included in the article's Creative Commons licence and your intended use is not permitted by statutory regulation or exceeds the permitted use, you will need to obtain permission directly from the copyright holder. To view a copy of this licence, visit <http://creativecommons.org/licenses/by/4.0/>.

© The Author(s) 2024